Time Correction of Ocean-Bottom Seismometers Using Improved Ambient Noise Cross Correlation of Multicomponents and Dual-Frequency Bands

Jinyu Tian[1], Jian Lin[1,2,3,4,5], Fan Zhang*[2,3], Min Xu[2,3], Yayun Zhang[2,3], Laiyin Guo[5], and Xin Zeng[2,3]

Abstract

An effective approach was developed for identifying and correcting ocean-bottom seismometer (OBS) time errors through improving ambient noise cross-correlation function (NCCF) analysis and combination with other methods. Significant improvements were illustrated through analyzing data from a passive-source seismic experiment in the southwestern sub-basin of the South China Sea. A novel method was first developed that can effectively identify errors in the sampling frequency of the OBS instruments. The traditional NCCF method was then expanded by increasing the analyzed data spectrum from a single-frequency band to dual-frequency band pairs, thus doubling the number of available data points and substantially improving the time correction quality. For data with relatively low signal-to-noise ratios, the average time errors were reduced from the original average values of 60–80 ms by the conventional methods to <40 ms using the improved approaches. The new multistep procedure developed in this study has general applicability to analysis of other OBS experiments. The demonstrated significant improvements in the data quality are critical for advancing seismic tomography and other modern marine geophysical studies that require high accuracy in the OBS data.

Cite this article as Tian, J., J. Lin, F. Zhang, M. Xu, Y. Zhang, L. Guo, and X. Zeng (2021). Time Correction of Ocean-Bottom Seismometers Using Improved Ambient Noise Cross Correlation of Multicomponents and Dual-Frequency Bands, *Seismol. Res. Lett.* **XX**, 1–11, doi: 10.1785/0220200358.

Introduction

Accurate time recording of seismic data is critically important in modern marine geophysical research, including high-resolution seismic tomography and earthquake relocation. For instance, for an ocean-bottom seismometer (OBS) array with 50 km average station distance, detecting a 1% velocity anomaly in seismic tomographic data requires a seismogram time accuracy of 62.5–125 ms (Le *et al.*, 2018). However, unlike land seismometers, for which recording times can be periodically calibrated via Global Positioning System (GPS), the clock inside an OBS can only be synchronized with an onboard GPS before deployment and after recovery. During OBS deployment, the timing of seismic records was determined by a quartz crystal oscillator inside the OBS. The oscillation frequency of the quartz can become unstable because of a range of factors, including temperature and pressure changes in the complex seafloor environment (Gardner and Collins, 2012; Hannemann *et al.*, 2014; Takeo *et al.*, 2014). Such time errors in seismic records are particularly problematic in conducting high-quality long-term passive-source OBS experiments.

Time errors in OBS records typically consist of static and dynamic components (Hannemann *et al.*, 2014; Le *et al.*, 2018; Liu *et al.*, 2018), which could be identified and corrected using multiple methods. Static errors (i.e., a constant offset with respect to a reference clock) can be corrected through GPS synchronization prior to the OBS deployment. Dynamic errors, which are time varying, have at least three causes as described as follows. (1) When an OBS was reset to enter a new sampling mode prior to deployment, the instrument will utilize a new oscillator sampling frequency, which could differ from the assigned OBS

1. State Key Laboratory of Marine Geology, School of Ocean and Earth Science, Tongji University, Shanghai, China; 2. Key Laboratory of Ocean and Marginal Sea Geology, South China Sea Institute of Oceanology, Innovation Academy of South China Sea Ecology and Environmental Engineering, Chinese Academy of Science, Guangzhou, China; 3. Southern Marine Science and Engineering Guangdong Laboratory, Guangzhou, China; 4. Department of Geology and Geophysics, Woods Hole Oceanographic Institution, Woods Hole, Massachusetts, U.S.A.; 5. Department of Ocean Science and Engineering, Southern University of Science and Technology, Shenzhen, China

*Corresponding author: zhangfan@scsio.ac.cn

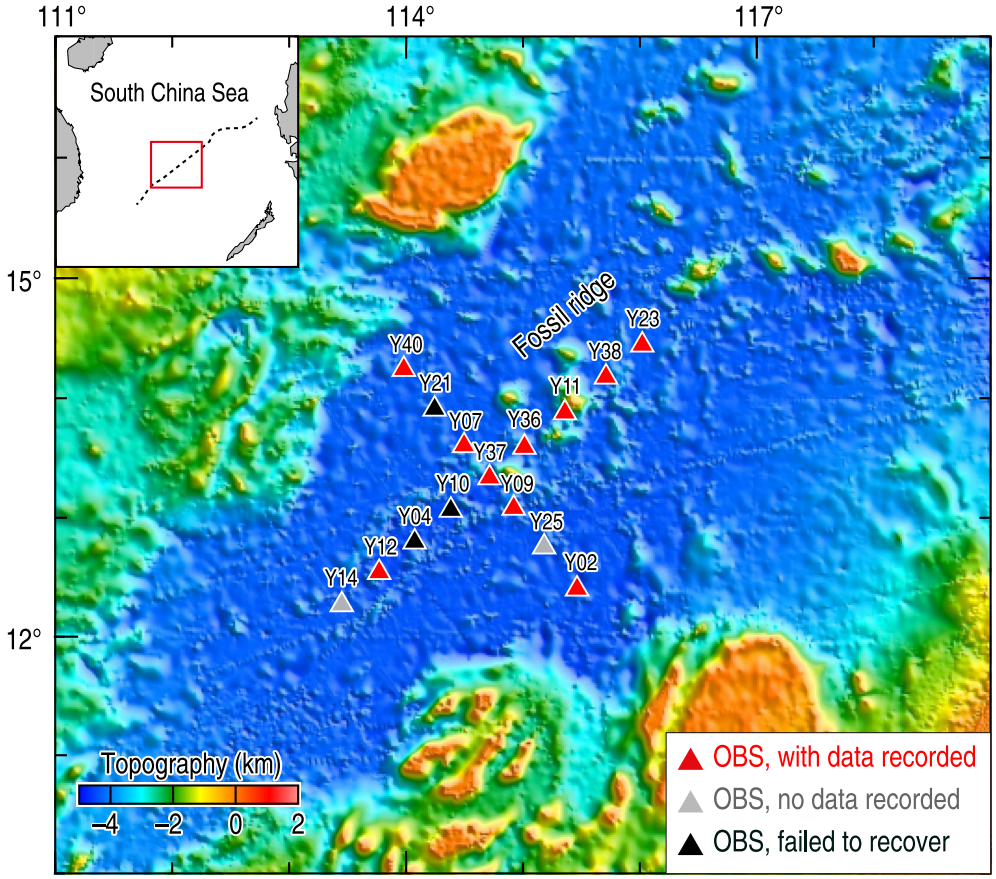

Figure 1. Locations of an array of 15 ocean-bottom seismometers (OBSs) deployed in the southwestern South China Sea (SCS) along and perpendicular to the fossil ridge (black dotted line in the inset). (Inset) Location of the study area (red frame). It was deployed from 20 June to 11 October 2017 by the R/V Shiyan 3 of the South China Sea Institute of Oceanography (SCSIO), Chinese Academy of Sciences. Red, black, and gray triangles indicate the locations of OBSs that recorded valid data used in this study were not recovered, and recorded no data, respectively. The color version of this figure is available only in the electronic edition.

standard sampling frequency, leading to a linear drift in the OBS time. (2) Compared with the room temperature conditions on the ship, the temperatures at the ocean bottom are relatively low, which could lead to a time drift on the OBS oscillator (Stähler *et al.*, 2016; Hable *et al.*, 2018). The cumulative time drift caused by such changes in the environmental conditions can be calculated and corrected using the skew values (i.e., the offset values of the OBS instrument with respect to the GPS checking before and after an OBS deployment), which are stored in the OBS instrumental log files. However, occasionally, the log files are lost because of power failure (Stähler *et al.*, 2016; Loviknes *et al.*, 2020), water leakage into instruments, or other unexpected factors. In such cases, it is necessary to identify and correct the time drift errors through other means. (3) Nonlinear time-varying errors may be caused by complex factors at the ocean bottom, including water pressure changes, random instrumental errors, and so on (Gardner and Collins, 2012; Hannemann *et al.*, 2014; Takeo *et al.*, 2014).

Another important method of time correction is the use of the asymmetry between causal and acausal signals from ambient noise cross-correlation function (NCCF). The principle of NCCF was proposed by Lobkis and Weaver (2001) and has been widely used in seismology, including investigations of local (Shapiro and Campillo, 2004; Shapiro *et al.*, 2005; Yao *et al.*, 2006; Harmon *et al.*, 2007; Takeo *et al.*, 2014) and global (Haned *et al.*, 2016) tomography, azimuthal anisotropy of the lithosphere (Yao *et al.*, 2010; Takeo *et al.*, 2014), and velocity structural changes around active volcanoes (Sens-Schönfelder and Wegler, 2006; Brenguier, Campillo, *et al.*, 2008; Sens-Schönfelder *et al.*, 2014) and tectonic faults (Brenguier, Shapiro, *et al.*, 2008; Wegler *et al.*, 2009).

The NCCF has been used to correct the time errors of both land stations (Stehly *et al.*, 2007; Sens-Schönfelder, 2008) and OBSs (Sabra *et al.*, 2005; Gouedard *et al.*, 2014; Hannemann *et al.*, 2014; Hable *et al.*, 2018; Le *et al.*, 2018). Xia *et al.* (2015) and Xie *et al.* (2018) used localized microseismic source signals in the NCCF to correct the time errors in instruments. Le *et al.* (2018) used Scholte waves (Scholte, 1947) from hydrophone signals to acquire NCCF signals with high signal-to-noise ratios (SNRs). Hable *et al.* (2018) used multicomponent NCCF for each station pair to reduce the standard deviation of the time error estimates. However, three problems can occur when using the traditional NCCF method for time correction. First, inaccurate time information stored in the data file can lead to nonlinear dynamic time errors, which are difficult to correct (Hable *et al.*, 2018; Le *et al.*, 2018; Zhu *et al.*, 2019, 2020). Second, the actual instrument sampling frequency can differ from the assigned frequency value, which might be unnoticed and thus lead to time errors. Third, if the SNRs of the NCCF are relatively low, it can be difficult to acquire sufficient station pairs to calculate time errors with relatively low standard deviations.

In this study, we developed a comprehensive new procedure to minimize OBS time errors. In step 1, we effectively used the

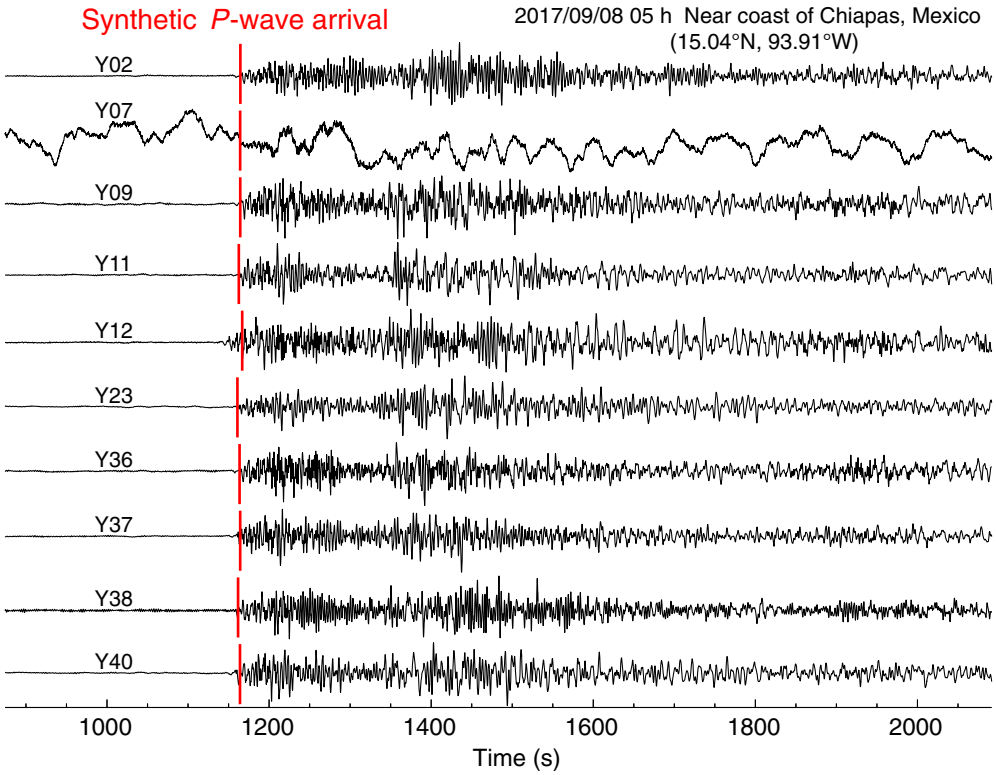

Figure 2. Vertical-component recorded from an earthquake that occurred near the coast of Mexico (15.04° N, 93.91° W) on 8 September 2017. Red lines show the synthetic arrival time of the *P* wave calculated based on the IASP91 model for all stations. The color version of this figure is available only in the electronic edition.

accurate time of OBSs, which were synchronized with GPS before deployment, to standardize the length of raw data files. In step 2, for OBSs with instrumental log files, time errors were calculated analytically using theoretical formula. In step 3, we used an improved NCCF analysis method by expanding the data pairs from a single- to dual-frequency bands to significantly increase the number of NCCF pairs. This new combined approach significantly improved the NCCF analysis with low SNRs. The much-improved dataset can be used in studies of high-resolution surface wave and teleseismic *P*-wave tomography.

Data Preprocessing

The data employed in this study were acquired from a passive-source seismic experiment conducted in the southwestern South China Sea (SCS) by the R/V Shiyan 3 in 2017. A total of 15 broadband OBSs of type I-4C with three-component sensors and a hydrophone (Ruan *et al.*, 2010) were deployed for six months in 3.5–4.5 km deep water near the fossil ridge in the southwestern sub-basin of the SCS (Fig. 1). Twelve OBSs were successfully recovered, of which two had no data recorded. During the SCS experiment, the OBS instruments were assigned sampling frequencies of either 100 or 50 Hz. The spacing of the stations ranged from 35 to 320 km with an average value of ~50 km.

To determine the time accuracy of the seismograms, errors were first estimated according to the synthetic arrival time of *P* phases based on the IASP91 Earth model (Kennett and Engdahl, 1991) using teleseismic data from the 8 September 2017 M_w 8.1 earthquake near the coast of Mexico (15.04° N, 93.91° W). All the seismograms had relatively high SNRs except for OBS Y07 (Fig. 2). Among the remaining OBSs, time errors were >20 s for OBSs Y12 and Y40, which required correction before further use.

Standardization of data length

Typically, seismic data files of 24 hr time-series are used in tomography studies. However, the time lengths of the original raw data files can vary among OBSs. For example, for the data with 100 Hz sampling frequency, the length of one raw data file is ~29 hr. Thus, the raw data files need to be first separated into lengths of 24 hr each. The time stored in the first raw data file was used as the absolute time, and then the data were divided based on a fixed number of sampling points. We assumed that the time-series records were uninterrupted, and thus there were no gaps between the two adjacent data files. If there were gaps caused by instrumental faults in the data, they should be identifiable by the existence of broken NCCF signals (see the Time Correction of Anomalous Sampling section). All the original files were stacked end to end by the recording sequence, and every 8,640,000 points (i.e., 24-hr long record assuming the data sampling frequency of 100 Hz) were cut into a series of new day-length data files (Fig. 3a). Using the previous approaches, we found that the sampling frequencies of the instruments used in the SCS experiment differed from the assigned frequencies, and the resultant time errors were corrected by the methods described in the following.

Time correction of anomalous sampling

After the data file lengths were cut correctly as described earlier, we next identified sampling anomalies in the data caused by instrumental faults. Two types of sampling anomalies were found in our dataset: (1) 5–8 min periodic recording jumps

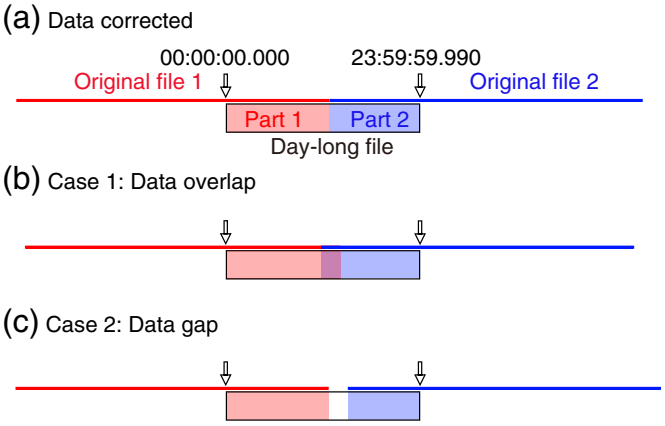

Figure 3. Illustration of the day-long data-cutting process. Red and blue lines show adjacent raw data files. Black boxes represent the day-long data after the cut. (a) The method used for data cutting in this study, which combines all raw data and then cut them by a fixed number of sampling points. (b,c) Cases of data overlap and gap cut using the regular method, which is based on the raw data header-file times. The color version of this figure is available only in the electronic edition.

every 4 hr caused by the instrumental faults in OBS Y23 and Y36, which were then corrected by interpolation, and (2) a data gap of 17,920 ms caused by instrumental malfunction was found in OBS Y12 (Fig. 4a,c), which was then corrected by filling zero values in which the data gap occurred (Fig. 4b,d).

New Methods for Time Correction

Correcting errors in sampling frequency using instrumental log files

Instrumental log files record important information, including the header-file time, the file name in format of hexadecimal number, the assigned sampling frequency, skew values based on GPS synchronization after recovery, and the time-control (TC) frequency value (Table 1). The TC frequency value was generated and recorded immediately when the OBS entered a new sampling mode. The TC frequency is a constant that determined the actual sampling frequency of the OBS in the current sampling mode. In general, there was a small deviation between the actual and the assigned sampling frequency, which caused linear time drifts in the data (PErr). The clock drift errors can be evaluated using equations (1) and (2) described in the following:

$$\mathrm{TErr} = \mathrm{PErr} + \mathrm{SErr}, \tag{1}$$

in which TErr is the total clock drift error of the OBS, which consists of two components PErr and SErr; PErr is the clock drift caused by the difference between the actual and assigned sample oscillator frequency; and SErr is the skew value, that is, the offset values of the OBS instrument with respect to the GPS checking before and after an OBS deployment.

$$\mathrm{PErr} = \left(\frac{TC}{256} - f_0\right) \times \left(\frac{\mathrm{NTFS}}{\mathrm{sps}}\right) \times \frac{1}{f_0}, \tag{2}$$

in which $f_0 = 12{,}288{,}000$ (Hz) is the standard sampling oscillator frequency of the I-4C type OBSs; NTFS is the number of sampling points; sps is the assigned sampling frequency (Hz); and the factor 256 is a dimensionless parameter for the I-4C-type OBS instrument (Liu *et al.*, 2018).

The correct time of each OBS was calculated for each sampling point using the TErr value. The uncertainty in the time correction of the OBSs that were analyzed by this method can be theoretically considered as zero. During the SCS experiment, the instrumental log files were available for most stations, and thus the previous correction method was applicable. However, OBS Y36 and Y37 were found to lack records of skew values caused by instrumental faults, so we can only use the NCCF method to correct time errors as described in the following.

Improved NCCF methods using multicomponents and dual-frequency bands

The time asymmetry of NCCF signals can be used for time correction. There are no active volcanoes or tectonic faults around the study region; therefore, the velocity changes in the Earth medium during our experiment should be negligible. Previous studies have indicated that compared with instrumental time errors, uneven distributions and temporal changes in noise sources have relatively little influence on the asymmetry of NCCF signals (Yao and van der Hilst, 2009; Le *et al.*, 2018). Therefore, OBS time errors were the main factor affecting the time symmetry of the NCCF signals.

To determine the time errors from NCCF signals with relatively low SNRs (<10), we developed an improved procedure using dual-frequency bands of the NCCF signals to increase the calculated pairs based on the multicomponent NCCF method (Hable *et al.*, 2018). We then used the weighted average equations (equations 3 and 4) (Hobiger *et al.*, 2012; Hable *et al.*, 2018) to calculate the time errors from multicomponents and dual-frequency band pairs:

$$\varepsilon(t) = \frac{\sum_{i=1}^{N} \mathrm{CC}_i^2(t) \times \varepsilon_i(t)}{\sum_{i=1}^{N} \mathrm{CC}_i^2(t)}, \tag{3}$$

$$\mathrm{CC}(t) = \frac{\sum_{i=1}^{N} \mathrm{CC}_i^3(t)}{\sum_{i=1}^{N} \mathrm{CC}_i^2(t)}, \tag{4}$$

in which ε denotes the best estimate of the time errors from all pairs; CC denotes the correlation coefficient value; ε_i and CC_i are the ε and CC of pair i, respectively; and N is the number of usable pairs.

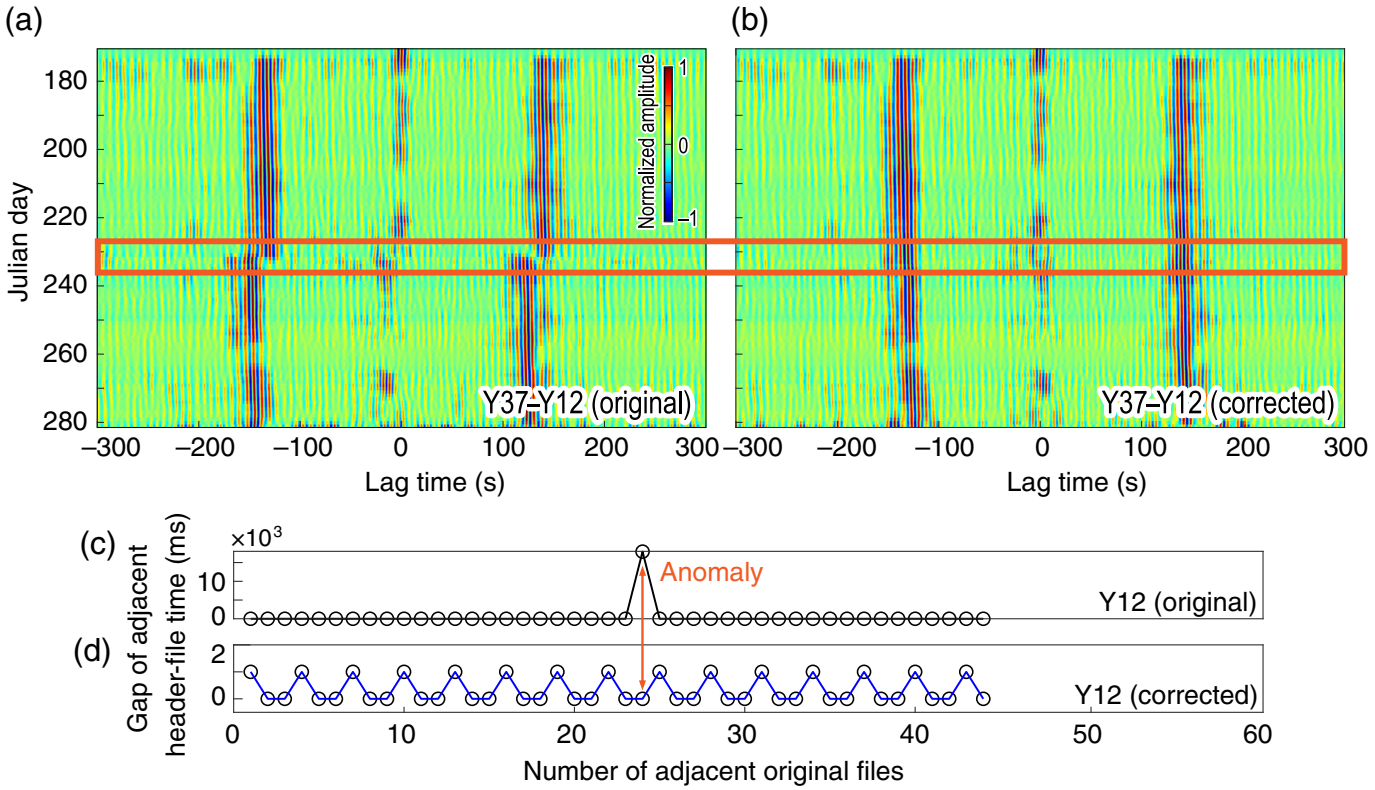

Figure 4. Data sampling anomaly correction. (a,c) Anomaly value of OBS Y12. After the gaps were filled with zero values, (b) the noise cross-correlation function (NCCF) signals and (d) gaps in the adjacent header-file times returned to normal. The color version of this figure is available only in the electronic edition.

Before calculating the NCCF, we followed the method of Bensen *et al.* (2007) and Yao *et al.* (2011) to preprocess the data, including removing the instrument response, mean value, and linear trend, as well as applying a band-pass filter. One-bit normalization and whitening were applied to the down-sampled data to remove the earthquake signals. The day-long time series were then divided into 2 hr windows to calculate the daily NCCFs. Zero-phase band-pass filters between 0.1–0.2

TABLE 1
Skew Values and Time-Control (TC) Values of All Stations

Station	Skew Values (s)	Time-Control Values (Hz)	Assigned Sampling Frequency (Hz)	Actual Sampling Frequency (Hz)	Time Drift Rate (ms/day)	Uncertainty σ (ms)
Y02	0.186105	3,145,727,796	100	99.99999541990	3.957	0
Y07	0.130458	3,145,728,620	100	100.0000210765	−18.210	0
Y09	0.111069	3,145,728,133	100	100.0000053894	−4.656	0
Y11	0.059704	3,145,727,920	100	99.99999807938	1.659	0
Y12	0.081730	3,145,727,830	50	49.99999772828	3.926	0
Y23	0.044418	3,145,728,096	100	100.0000035134	−3.036	0
Y36	—	3,145,727,518	100	99.99999267297	6.336	41.7
Y37	—	3,145,725,346	50	49.99995881461	68.092	37.0
Y38	0.193449	3,145,725,313	100	99.99991659656	72.061	0
Y40	0.163275	3,145,725,191	100	99.99991242224	75.667	0

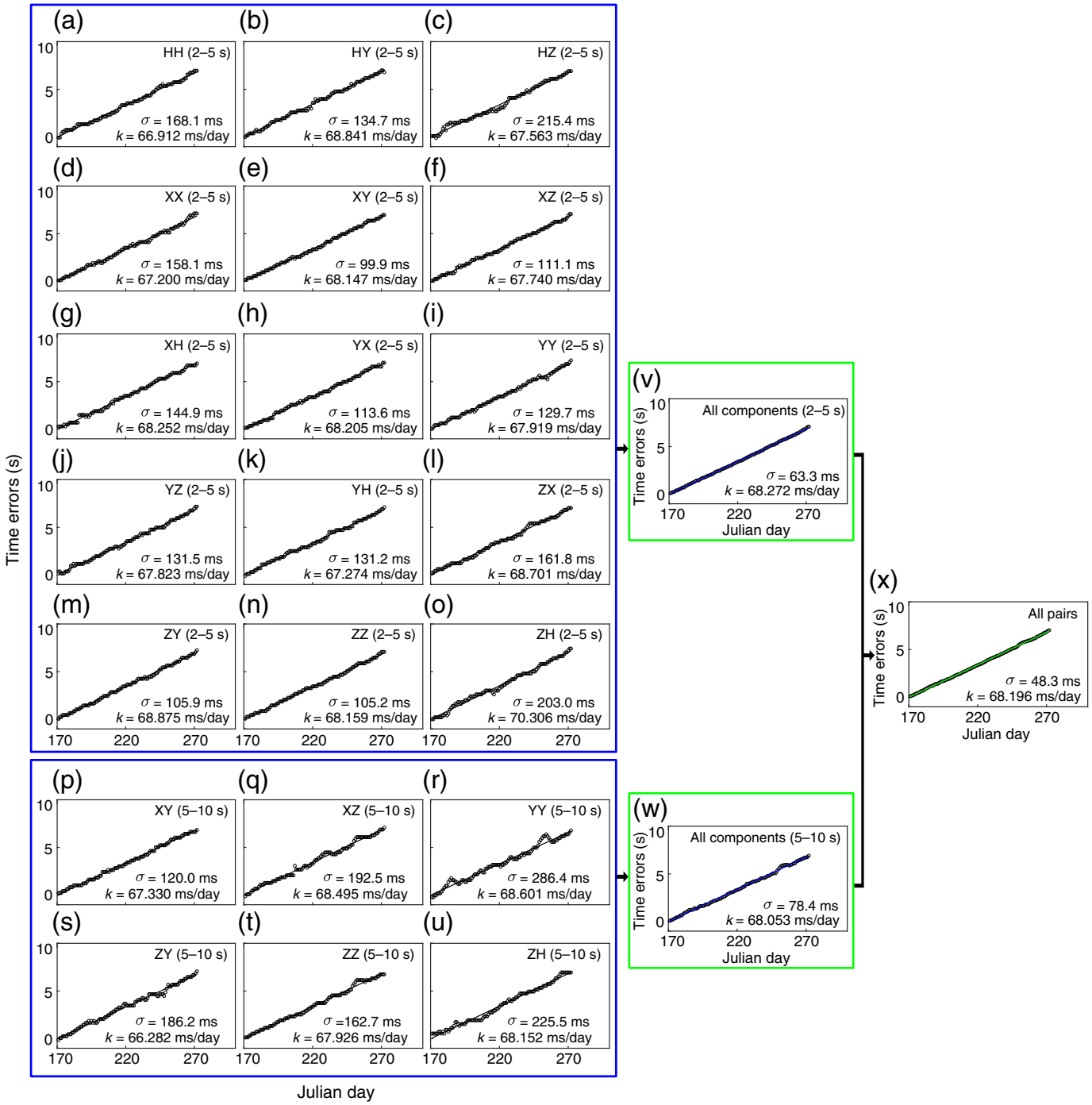

and 0.2–0.5 Hz were applied to create two frequency bands for analysis.

The time errors between two stations were determined from the NCCF signals and were fitted using linear functions (Figs. 5 and 6). The standard deviation of linear time drifts was significantly reduced by adding the new frequency band pairs (Fig. 5 and Table 2). For example, the relative time errors of the station pair Y37–Y09 from Julian days 170–270 were estimated by the cross correlation of multicomponents and dual-frequency band pairs. The standard deviations were estimated to be 60–80 ms (Fig. 5v,w) by averaging the individual Y37–Y09

Figure 5. Relative time errors of OBSs Y37–Y09 from Julian days 170 to 270 in 2017, estimated from the cross correlations of multiple-component pairs and period-band pairs. Panels (v) and (w), in blue lines, show the time errors estimated by averaging the individual Y37–Y09 component pairs in the period bands of (a–o) 2–5 s and (p–u) 5–10 s. The standard deviations σ (ms) and rate of time drift k are shown to the right of each panel. The σ values were much lower in panel (x) than in any of the individual pairs in panels (a–w). The color version of this figure is available only in the electronic edition.

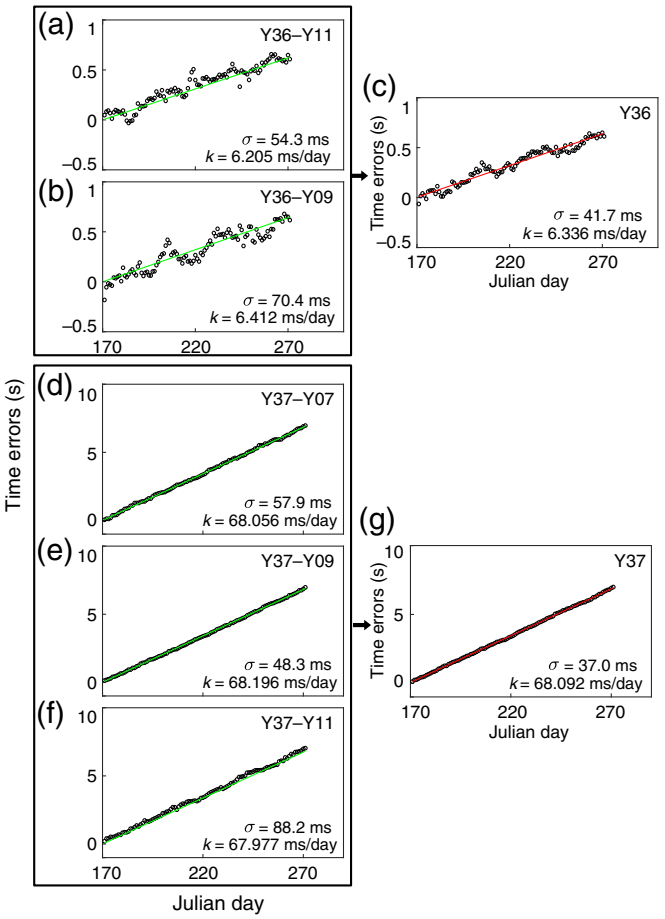

Figure 6. Time errors of OBSs Y36 and Y37, estimated by cross correlation of station pairs following the procedure in Figure 5. The results for (a) Y36–Y11, (b) Y36–Y09, (d) Y37–Y07, (e) Y37–Y09, and (f) Y37–Y11 are similar to those shown in Figure 5x. The time errors of (c) Y36 and (g) Y37 in all panels are fitted with linear functions (red curves). The color version of this figure is available only in the electronic edition.

component pairs in the frequency band of 2–5 s (Fig. 5a–o, σ = 100–220 ms) and 5–10 s (Fig. 5p–u, σ = 120–280 ms). After averaging the results from the component pairs of the dual-frequency bands, the values were reduced to 48.3 ms (Fig. 5x).

Within an OBS station pair (e.g., Y09 and Y36), the instrument that has already been corrected for the time drifts based on the instrumental log file as described earlier (e.g., Y09) was used as the reference station; the calculated time errors between Y36–Y09 based on the NCCF analysis were then assigned as the time error for station Y36. After taking the weighted average of two station pairs for Y36 (Fig. 6c, σ = 41.7 ms) and three station pairs for Y37 (Fig. 6g, σ = 37.0 ms), the standard deviations of the time drifts were much lower than those obtained from the individual station pair (Fig. 6a, Y36–Y11, σ = 54.3 ms; Fig. 6b, Y36–Y09, σ = 70.4 ms; Fig. 6d, Y37–Y07, σ = 57.9 ms; Fig. 6e, Y37–Y09, σ = 48.3 ms; and Fig. 6f, Y37–Y11, σ = 88.2 ms). The time drift estimates for individual stations were further improved by averaging all station pairs (Table 2). The actual sampling frequency of OBSs, final time drifts, and accuracy are listed in Table 1.

Discussion

How to standardize the length of the data

In traditional methods, the starting time stored in header file of each data file was used to divide the raw data into day-long time series. However, the time difference between the two adjacent header files does not equal to the time length (i.e., the sampling points times sampling frequency) of the front file; therefore, if the raw header information was used to separate the data files, data overlap or gap could occur (Fig. 3b,c). This error cannot be simply corrected by removing repeated data points or interpolating missing ones. Thus, in this study, we used the starting time of the first header file together with a fixed number of sampling points to complete this correction. Two examples are given to explain the advantages of the

TABLE 2
Comparison of the Uncertainty in Single- and Dual-Frequency Band Noise Cross-Correlation Functions (NCCFs)

Station Pair	Single-Frequency Band (2–5 s) (ms)	Single-Frequency Band (5–10 s) (ms)	Dual-Frequency Bands (ms)
Y37–Y07	68.6	88.2	57.9
Y37–Y09	63.3	78.4	48.3
Y37–Y11	105.9	117.7	88.2
Y37	**59.8**	**70.5**	**37.0**
Y36–Y09	82.3	102.1	70.4
Y36–Y11	67.9	90.0	54.3
Y36	**60.3**	**81.4**	**41.7**

The nonbold values in this table present the uncertainties of station pairs and the bold values present the final uncertainties of Y36 and Y37.

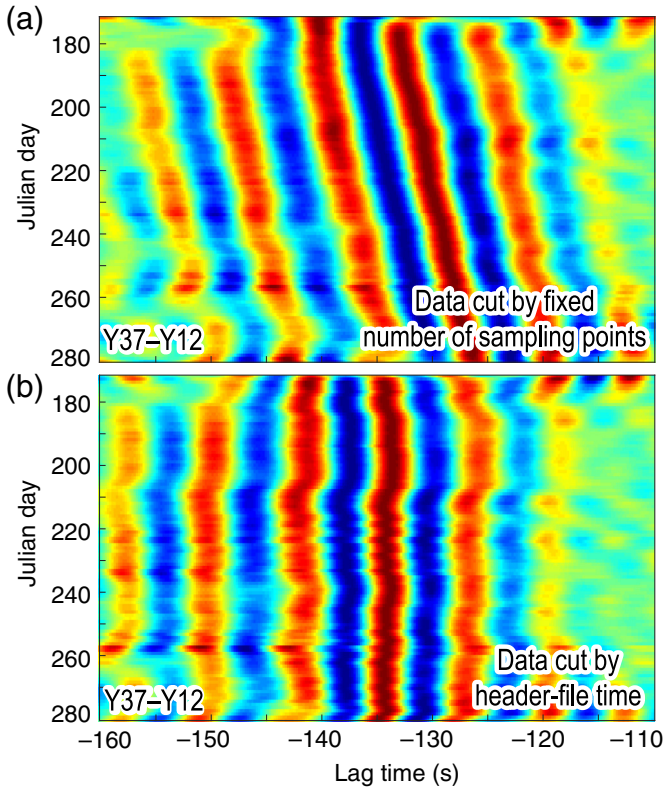

Figure 7. NCCF signals of an example station pair (Y37–Y12) following two methods of cutting day-long time series. (a) Linear time drifts in the NCCF signals. Data were cut based on the first raw header-file time and a fixed number of sampling points. (b) Nonlinear time errors. Data were cut based on every raw data header-file time. Color scales are the same as in Figure 4. The color version of this figure is available only in the electronic edition.

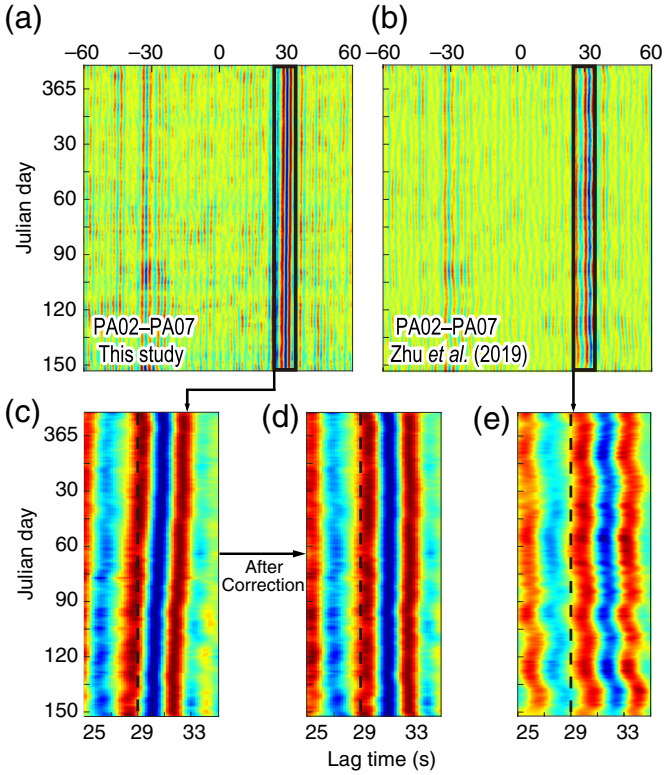

Figure 8. Comparison of NCCF signals from hydrophone recordings at OBSs PA02–PA07 from (a) this study and (b) Zhu *et al.* (2019). Perfectly linear time errors appeared in panel (c) and time errors were small in panel (d) compared with the poor linear time errors in panel (e). Color scales are the same as in Figure 4. The color version of this figure is available only in the electronic edition.

data-cutting process used in this study (Figs. 7 and 8). First, we cut the same data of OBS Y12 and Y37 in two ways and calculated the NCCF signals. The time errors were mostly linear in the NCCF signals (Fig. 7a) when cut the data using the method of this study, and thus more accurate clock drifts can be determined. In contrast, if the data were cut using the traditional method of considering only the header-file times, there were obvious nonlinear time errors (Fig. 7b). The resulting time series would be inaccurate if these were assumed to be linear time drifts. Second, we also cut the day-long time series and corrected the time errors for the same data as that used by Zhu *et al.* (2019). The types of the OBS sensors used in Zhu *et al.* (2019) are the same as in this study, while the OBS data of Zhu *et al.* (2019) were acquired from another experiment at the southern Mariana trench. It is seen that the new data-cutting method of this study could acquire almost perfect linear time drifts (Fig. 8a,c) with standard deviations as low as 25 ms (Fig. 9, in red circles); in contrast, the data cutting using the erroneous times in the header files would lead to nonlinear time errors (Fig. 8b,e) with standard deviations of ~200 ms (Fig. 9, in black crosses) as reported by Zhu *et al.* (2019). Thus, the time accuracy was improved eightfold using the new method.

Importance of calculating actual instrument sampling frequency

During an experiment, the data recording sampling frequency is generally determined before deployment based on an assigned sampling frequency. If we cut the day-long time series by a fixed number of sampling points and the assigned sampling frequency, there should be no time errors. However, linear time drifts appeared in the NCCF signals (Figs. 7a and 8c), which can result from a small deviation between the actual and assigned sampling frequency. Such small deviation is shown by the observation that the actual sampling frequency of each OBS calculated using its own instrumental log file was different from that of the standard sample oscillator frequency (12,288,000 Hz) of the I-4C type OBSs (Table 1).

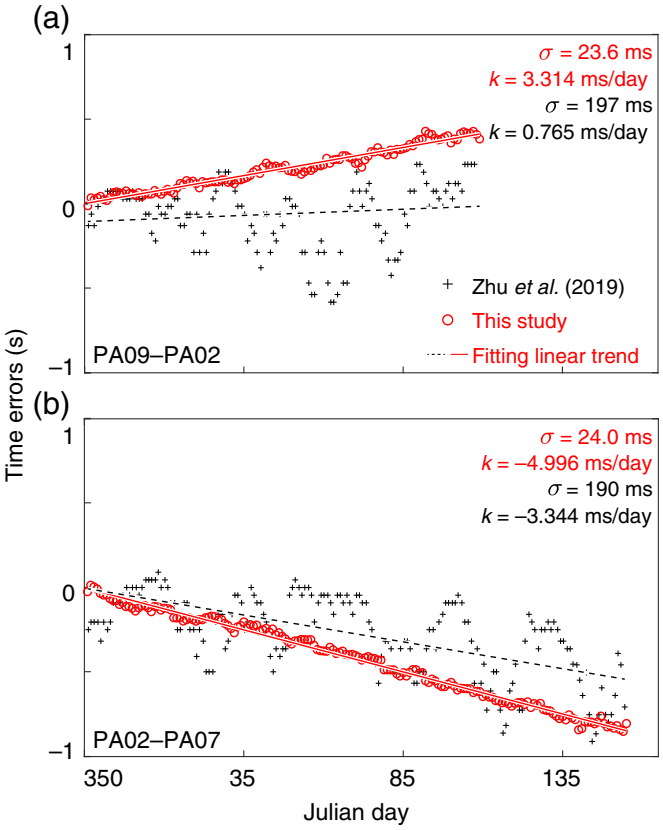

Figure 9. Comparison of time errors estimated at the (a) PA09–PA02 and (b) PA02–PA07 station pairs in this study (red circles) and by Zhu *et al.* (2019; black crosses). The errors of the present study and of Zhu *et al.* (2019) are fitted with linear functions (red and black curves, respectively). Note that the standard deviations σ are only ~20–30 ms. The color version of this figure is available only in the electronic edition.

Comparison with the time accuracy of other studies

Hable *et al.* (2018) presented an effective method for correcting the time errors of OBSs with high SNRs. However, for the individual station pairs with low SNRs used in our study, a time accuracy of 60–80 ms (Fig. 5v,w) was acquired using the method of Hable *et al.* (2018). After adding more available frequency band pairs of NCCFs, the accuracy was improved by 1.5–2.0 times (Fig. 5x and Table 2).

For surface wave and teleseismic *P*-wave tomography, the data from all stations should meet the time accuracy requirement, which is anticorrelated with station distance (Fig. 10, Le *et al.*, 2018). For instance, OBSs with interstation distances of 100 km should have time accuracies of 0.25 and 0.125 s for surface wave and teleseismic *P*-wave tomography, respectively (Fig. 10). Hannemann *et al.* (2014), Hable *et al.* (2018), Le *et al.* (2018), and Zhu *et al.* (2019) reported standard deviations of 87–129, 200, 8.4–43.9, and 160–245 ms for interstation distances of ~75, 60–270, 16–374, and 37–83 km, respectively

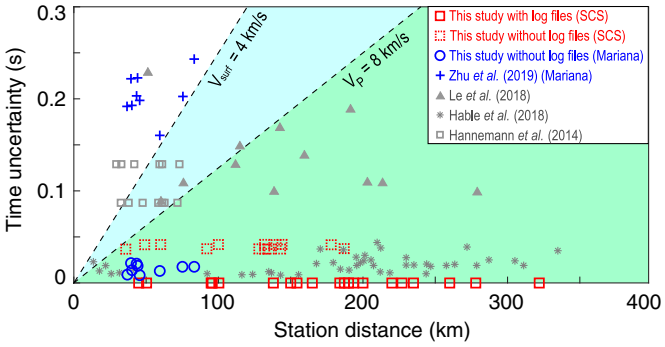

Figure 10. Comparison with previous studies (gray markers). Black-dotted lines and shadows show the time accuracy requirements in surface and *P*-wave tomography. In the southern Mariana data of Zhu *et al.* (2019), the standard deviations are 160–245 ms (crosses). We achieved improved accuracy of only 20–30 ms for the same southern Mariana data (blue circles) and ~40 ms for the SCS data (red squares). The color version of this figure is available only in the electronic edition.

(Fig. 10). In this study, for OBSs containing instrumental log files, the time errors can be reduced to 0 ms (Fig. 10, solid red squares). Meanwhile, for OBSs without instrumental log files, the time errors can be reduced to 25–40 ms, depending on the SNRs (Fig. 10, dotted red squares). Our results demonstrate that time correction using instrumental log files and multicomponents and dual-frequency bands noise cross correlation significantly improved the time accuracy, especially for data with low SNRs.

Conclusions

In this study, we developed multiple methods to identify, estimate, and correct instrumental time errors for any type of OBS. Our investigation reveals that a combination of the following methods significantly reduces OBS time errors:

1. An effective method was employed to standardize the raw data files. This method is efficient in removing the influence of the nonlinear time errors, which exist in the header files, thus facilitating time error correction.
2. Instrumental log file correction and ambient NCCF were combined to identify time errors. For the NCCF analysis, we used a method of comparing multicomponents, dual-frequency bands, and station pairs to enable efficient correction of systematic linear time errors.
3. The combination of the previous methods reduced the average time accuracy to 0–40 and 0–25 ms for data with low and high SNRs, respectively, which is significantly better than that of previous studies (up to 200 ms).

The new combined data correction methods proposed in this study have general applicability to analysis of other OBS experiments.

Data and Resources

The codes for computing time correction are available upon request to the first author (jytian0419@gmail.com). Seismic Analysis Code (SAC) was used in this study (Goldstein *et al.*, 2003). Seismograms used in this study were collected during a passive-source seismic experiment conducted in the southwestern South China Sea (SCS) by the R/V Shiyan 3 in 2017 and cannot yet be released to the public. The map was made with Generic Mapping Tools (Wessel *et al.*, 2013).

Acknowledgments

The authors are grateful to Editor Allison Bent, Reviewer Joshua Russell, and an anonymous reviewer for their constructive comments that have improved this article. The authors thank Huajian Yao for providing the noise cross-correlation function (NCCF) codes; Doug Wiens for suggestions that significantly improved this article; and Hongfeng Yang, Yunlong Liu, Yong Zhou, Xubo Zhang, and Gaohua Zhu for stimulating discussion. The authors express sincere appreciation to the science party and crew of the R/V Shiyan 3 for deployment and recovery of the ocean-bottom seismometer (OBS) instruments during the South China Sea (SCS) and Mariana expeditions. This study was supported by the National Natural Science Foundation of China (91858207, 41890813, 91628301, 41976064, 91958211, and U1606401), the International Exchange Program for Graduate Students of Tongji University (201901255), the Chinese Academy of Sciences (Y4SL021001, QYZDY-SSW-DQC005, and 133244KYSB20180029), the Southern Marine Science and Engineering Guangdong Laboratory (Guangzhou, GML2019ZD0205), and the National Key R&D Program of China (2018FY100505).

References

Bensen, G. D., M. H. Ritzwoller, M. P. Barmin, A. L. Levshin, F. Lin, M. P. Moschetti, N. M. Shapiro, and Y. Yang (2007). Processing seismic ambient noise data to obtain reliable broad-band surface wave dispersion measurements, *Geophys. J. Int.* **169,** no. 3, 1239–1260.

Brenguier, F., M. Campillo, C. Hadziioannou, N. M. Shapiro, R. M. Nadeau, and E. Larose (2008). Postseismic relaxation along the San Andreas fault at Parkfield from continuous seismological observations, *Science* **321,** no. 5895, 1478–1481.

Brenguier, F., N. M. Shapiro, M. Campillo, V. Ferrazzini, Z. Duputel, O. Coutant, and A. Nercessian (2008). Towards forecasting volcanic eruptions using seismic noise, *Nature Geosci.* **1,** 126–130.

Gardner, A. T., and J. A. Collins (2012). Advancements in high-performance timing for long term underwater experiments: A comparison of chip scale atomic clocks to traditional microprocessor-compensated crystal oscillators, *2012 Oceans*, IEEE, Hampton Roads, Virginia, 1–8.

Goldstein, P., D. Dodge, M. Firpo, and L. Minner (2003). SAC2000: Signal processing and analysis tools for seismologists and engineers, in *Invited contribution to The IASPEI International Handbook of Earthquake and Engineering Seismology*, W. H. K. Lee, H. Kanamori, P. C. Jennings, and C. Kisslinger (Editors), Academic Press, London, United Kingdom.

Gouedard, P., T. Seher, J. J. Mcguire, J. A. Collins, and R. D. van der Hilst (2014). Correction of ocean-bottom seismometer instrumental clock errors using ambient seismic noise, *Bull. Seismol. Soc. Am.* **104,** no. 3, 1276–1288.

Hable, S., K. Sigloch, G. Barruol, S. C. Stähler, and C. Hadziioannou (2018). Clock errors in land and ocean bottom seismograms: High-Accuracy estimates from multiple-component noise cross-correlations, *Geophys. J. Int.* **214,** no. 3, 2014–2034.

Haned, A., E. Stutzmann, M. Schimmel, S. Kiselev, A. Davaille, and A. Yelles-Chaouche (2016). Global tomography using seismic hum, *Geophys. J. Int.* **204,** no. 2, 1222–1236.

Hannemann, K., F. Krüger, and T. Dahm (2014). Measuring of clock drift rates and static time offsets of ocean bottom stations by means of ambient noise, *Geophys. J. Int.* **196,** no. 2, 1034–1042.

Harmon, N., D. Forsyth, and S. Webb (2007). Using ambient seismic noise to determine short-period phase velocities and shallow shear velocities in young oceanic lithosphere, *Bull. Seismol. Soc. Am.* **97,** 2009–2023.

Hobiger, M., U. Wegler, K. Shiomi, and H. Nakahara (2012). Coseismic and postseismic elastic wave velocity variations caused by the 2008 Iwate–Miyagi Nairiku earthquake, Japan, *J. Geophys. Res.* **117,** no. B09313, doi: 10.1029/2012JB009402.

Kennett, B. L. N., and E. R. Engdahl (1991). Traveltimes for global earthquake location and phase identification, *Geophys. J. Int.* **105,** no. 2, 429–465.

Le, B. M., T. Yang, Y. J. Chen, and H. Yao (2018). Correction of OBS clock errors using Scholte waves retrieved from cross-correlating hydrophone recordings, *Geophys. J. Int.* **212,** no. 2, 891–899.

Liu, Y., C. Liu, C. Tao, H. Yao, L. Qiu, A. Wang, A. Ruan, H. Wang, J. Zhou, and H. Li (2018). Time correction of the ocean bottom seismometers deployed at the southwest Indian ridge using ambient noise cross-correlation, *Acta Oceanol. Sin.* **37,** 39–46.

Lobkis, O. I., and R. L. Weaver (2001). On the emergence of the Green's function in the correlations of a diffuse field, *J. Acoust. Soc. Am.* **110,** no. 6, 3011–3017.

Loviknes, K., Z. Jeddi, L. Ottemöller, and T. Barreyre (2020). When clocks are not working: OBS time correction, *Seismol. Res. Lett.* **91,** no. 4, 2247–2258.

Ruan, A., J. Li, and Y. Chen (2010). The experiment of broad band I-4C type OBS in the Southwest Indian Ridge, *Chin. J. Geophys.* **53,** no. 4, 1015–1018 (in Chinese).

Sabra, K. G., P. Roux, A. M. Thode, G. L. D'Spain, W. S. Hodgkiss, and W. A. Kuperman (2005). Using ocean ambient noise for array self-localization and self-synchronization, *IEEE J. Ocean. Eng.* **30,** no. 2, 338–347.

Scholte, J. G. (1947). The range of existence of Rayleigh and Stoneley waves, *Geophys. J. Int.* **5,** no. 5, 120–126.

Sens-Schönfelder, C. (2008). Synchronizing seismic networks with ambient noise, *Geophys. J. Int.* **174,** no. 3, 966–970.

Sens-Schönfelder, C., E. Pomponi, and A. Peltier (2014). Dynamics of Piton de la Fournaise volcano observed by passive image interferometry with multiple references, *J. Volcanol. Geoth. Res.* **276,** 32–45.

Sens-Schönfelder, C., and U. Wegler (2006). Passive image interferometry and seasonal variations of seismic velocities at Merapi Volcano, Indonesia, *Geophys. Res. Lett.* **33,** no. 21, L21302, doi: 10.1029/2006GL027797.

Shapiro, N. M., and M. Campillo (2004). Emergence of broadband Rayleigh waves from correlations of the ambient seismic noise, *Geophys. Res. Lett.* **31,** no. 7, L07614, doi: 10.1029/2004GL019491.

Shapiro, N. M., M. Campillo, L. Stehly, and M. H. Ritzwoller (2005). High-resolution surface-wave tomography from ambient seismic noise, *Science* **307,** no. 5715, 1615–1618.

Stähler, S. C., K. Sigloch, K. Hosseini, W. C. Crawford, G. Barruol, M. C. Schmidt-Aursch, M. Tsekhmistrenko, J.-R. Scholz, A. Mazzullo, and M. Deen (2016). Performance report of the RHUM-RUM ocean bottom seismometer network around La Réunion, western Indian Ocean, *Adv. Geosci.* **41,** 43–63.

Stehly, L., M. Campillo, and N. M. Shapiro (2007). Traveltime measurements from noise correlation: Stability and detection of instrumental time-shifts, *Geophys. J. Int.* **171,** no. 1, 223–230.

Takeo, A., D. W. Forsyth, D. S. Weeraratne, and K. Nishida (2014). Estimation of azimuthal anisotropy in the NW Pacific from seismic ambient noise in seafloor records, *Geophys. J. Int.* **199,** no. 1, 11–22.

Wegler, U., H. Nakahara, C. Sens-Schönfelder, M. Korn, and K. Shiomi (2009). Sudden drop of seismic velocity after the 2004 M_w 6.6 mid-Niigata earthquake, Japan, observed with passive image interferometry, *J. Geophys. Res.* **114,** no. B06305, doi: 10.1029/2008JB005869.

Wessel, P., W. H. F. Smith, R. Scharroo, J. Luis, and F. Wobbe (2013). Generic Mapping Tools: Improved version released, *Eos Trans. AGU* **94,** no. 45, 409–410.

Xia, Y., S. Ni, X. Zeng, J. Xie, B. Wang, and S. Yuan (2015). Synchronizing intercontinental seismic networks using the 26 s persistent localized microseismic source, *Bull. Seismol. Soc. Am.* **105,** no. 4, 2101–2108.

Xie, J., S. Ni, R. Chu, and Y. Xia (2018). Assessing the short-term clock drift of early broadband stations with burst events of the 26 s persistent and localized microseism, *Geophys. J. Int.* **212,** no. 1, 324–332.

Yao, H., P. Gouédard, J. A. Collins, J. J. Mcguire, and R. D. van der Hilst (2011). Structure of young East Pacific Rise lithosphere from ambient noise correlation analysis of fundamental- and higher-mode Scholte–Rayleigh waves, *Compt. Rendus Geosci.* **343,** no. 8, 571–583.

Yao, H., and R. D. van der Hilst (2009). Analysis of ambient noise energy distribution and phase velocity bias in ambient noise tomography, with application to SE Tibet, *Geophys. J. Int.* **179,** no. 2, 1113–1132.

Yao, H., R. D. van der Hilst, and M. V. de Hoop (2006). Surface-wave array tomography in SE Tibet from ambient seismic noise and two-station analysis—I. Phase velocity maps, *Geophys. J. Int.* **166,** no. 2, 732–744.

Yao, H., R. D. van der Hilst, and J.-P. Montagner (2010). Heterogeneity and anisotropy of the lithosphere of SE Tibet from surface wave array tomography, *J. Geophys. Res.* **115,** no. B12307, doi: 10.1029/2009JB007142.

Zhu, G., H. Yang, J. Lin, and Q. You (2020). Determining the orientation of ocean-bottom seismometers on the seafloor and correcting for polarity flipping via polarization analysis and waveform modeling, *Seismol. Res. Lett.* **91,** no. 2A, 814–825.

Zhu, G., H. Yang, J. Lin, Z. Zhou, M. Xu, J. Sun, and K. Wan (2019). Along-strike variation in slab geometry at the southern Mariana subduction zone revealed by seismicity through ocean bottom seismic experiments, *Geophys. J. Int.* **218,** no. 3, 2122–2135.

Manuscript received 1 October 2020
Published online 13 January 2021